RSC Advances

This article can be cited before page numbers have been issued, to do this please use: A. Kool, P. Thakur, B. Bagchi, N. A. Hoque, S. Banerjee and S. Das, *RSC Adv.*, 2015, DOI: 10.1039/C5RA21091G.

View Article Online
DOI: 10.1039/C5RA21091G

Sol-gel synthesis of transition metal ions conjugated alumina rich mullite nanocomposites with potential mechanical, dielectric and photoluminescence properties

Arpan Kool[1], Pradip Thakur[1,2], Biswajoy Bagchi [3], Nur Amin Hoque[1], Somtirtha Banerjee[1], Sukhen Das[1,4]*

[1]Department of Physics, Jadavpur University, Kolkata- 700032, India

[2] Department of Physics, Netaji Nagar College for Women, Kolkata-700092, India.

[3] Fuel Cell and Battery Division, Central Glass and Ceramic Research Institute, Kolkata- 700032, India.

[4] Department of Physics, IIEST, Howrah, West Bengal - 711103, India.

*Corresponding author Email address: sdasphysics@gmail.com

ABSTRACT:

Nanocrystalline mullite have been synthesized from non-stoichiometric alkoxide precursors via sol gel route with Co^{2+}, Ni^{2+} and Cu^{2+} as dopant metal ions. Transition metal aluminate spinel phases, formed from the reaction between dopant metal ions and dissolved alumina species, introduced prominent colors to the composites after sintering. Interesting colors combined with suitable densification lead these composites to have potential use as ceramic pigments. A comparative Vickers and Knoop hardness have been evaluated in terms of dislocation movement along grain boundaries with highest hardness and Young's modulus values of ~8.7 GPa and ~207 GPa for copper and cobalt incorporated mullite respectively. Greater porosity of pure mullite results in an unconventionally high dielectric constant ~ 91 whereas larger interfacial polarization is responsible for the dielectric response of transition metal incorporated mullite composites. Formation of oxygen like defects in the composites cause prominent PL bands with highest PL intensity for dopant cobalt ions in mullite matrix.

Keywords: Composites; mullite; hardness; dielectric; photoluminescence.

View Article Online
DOI: 10.1039/C5RA21091G

1. Introduction:

Over last few years, the only stable aluminosilicate phase in high temperature solid state reaction between alumina and silica namely mullite has been used not only as traditional ceramics but as a functional ceramic too.[1,2] Mullite has become a good choice of ceramic material with electronic, optical and high temperature structural applications.[3] Owing to its unique properties like high melting point, high temperature strength, excellent chemical and thermal stability, low thermal conductivity, thermal expansion coefficient and dielectric constant, high transmittance in mid infrared region, mullite has got emerging engineering applications like components in reinforced composites, thermal barrier, ceramic capacitors, electronic packaging materials, window material in mid-infrared range, insulating material in spark plugs etc.[4-6]

Mullite comes with the general formula $Al^{VI}_2[Al^{IV}_{2+2x}Si_{2-2x}]O_{10-x}\otimes_x$ where IV and VI represent four and six fold coordination of aluminium cation respectively, $\otimes$ denotes an oxygen vacancy and x indicates the number of missing oxygen atoms per average unit cell with its value ranging between 0 and 1. The end member with x=0 corresponds to Al_2SiO_5 polymorphs like sillimanite, andalusite, and kyanite (mole ratio of Al/Si=2/1) which are perfectly crystalline states whereas for x=1, the other end member leads to a silica-free phase known as iota-alumina (ι-Al_2O_3).[7] Although any mullite composition between sillimanite and ι-Al2O3 is possible theoretically, mullite phases commonly fall into the range $0.18 \leq x \leq 0.88$. Among them frequently referenced mullite comes with four separate species differing in mole ratio between alumina and silica namely 3:2 mullite (x=0.25), 2:1 mullite (x=0.4), 4:1 mullite (x=0.67) and 9:1 mullite (x=0.842).[7,8]

The properties and microstructures of mullite are closely related to the synthesis routes employed and the type of precursor phases.[10] A large number of synthesis procedures of mullite have been reported till days among which thermal decomposition of natural aluminosilicates, sol-gel synthesis, hydrothermal procedures, molten salt synthesis, sintering of Al_2O_3 and SiO_2 powders, chemical vapor deposition and spray pyrolysis are most frequently undertaken ones.[11] Sol-gel synthesis has been a well established promising technique to fabricate high purity mullite composites resulting from the precursor with high degree of homogeneity and homogeneous distribution of components due to nanoscale mixing.[12] Different silicon and aluminum sources have been used for the mullite precursor synthesis. The most common precursor is a metal inorganic salt (acetate, chloride, nitrate, sulfate etc.) or an organic species like metal alkoxide. The metallic alkoxides are very favourable class of precursors used to obtain high performance mullite with desirable physico-chemical properties. During the sol-gel synthesis of mullite precursor from metal alkoxides, the alkoxides are hydrolysed first followed by a polymerization process and finally the precursor turns into well crystalline mullite upon high temperature sintering via nucleation and growth mechanism.

Different transition metals have strong mineralizing effect on the mullitization reaction with an decrease of the surface area and the pore volume.[13,14] These transition metal ions distort the local ligand symmetry (Jahn-Teller distortion) and they interact with the silica layer and destabilize

View Article Online
DOI: 10.1039/C5RA21091G

the aluminosilicate matrix which results in accelerated phase transformation. Moreover, the transition metal ions in form of oxides provide liquid phase at higher temperature which in turn increase the rate of dissolution of alumina into silica flux thus favouring the mullitization reaction sequences.[15, 16]

Although the effect of transition metal ions on the formation and microstructure of mullite has been very well established, [17-19, 10] their effect on the mechanical and photoluminescence properties of the same are rarely studied. Elastic modulus and hardness are two essential parameters for structural materials. It was evident that formation of dislocation networks within matrix grains and strengthened grain boundaries contribute to the mechanical strength of a composite.[20] Proper doping and formation of other crystalline phases within the matrix may also contribute to the higher microhardness and elastic modulus of mullite for which it can be used as structural ceramics. PL emission bands of alumina are reported to be closely related to oxygen related defects or F+ centres (oxygen vacancies with one-electron centers) and hence Al-rich or silicon deficient nanocrystalline mullite may also exhibit photoluminescence bands due to formation of oxygen vacancies.[2, 21-23]

Mullite without any mineralizer exhibit a low dielectric constant (~7) but its composites with alumina, cordierite or transition metals show promising dielectric characteristics.[2, 24, 25] The enhancement of dielectric constant for these types of composites can be attributed to the increased polarization due to presence of other crystalline phases and mobile charge carriers.

The degenerate d-orbitals of transition metal ions interact with the electron cloud of ligands to create a non-degeneracy of the d-orbitals. The visible light absorption band of any transition metal ions corresponds to the energy required to excite an electron from the t_{2g} level to the e_g level. Therefore, transition metal ion incorporated ceramic matrix can be used as stable ceramic pigments due to ability of transition metal compounds to show vivid colours and stability of ceramics at high temperatures.[26, 27] Moreover, transition metal aluminate phases (spinel phases) can be formed during sintering of mullite precursors with proper amount of dopant ions since divalent metal ions not being incorporated into mullite structure due to their large ionic radii, react with alumina to form aluminate phases.[27, 28] $CoAl_2O_4$, $NiAl_2O_4$ and $CuAl_2O_4$ posses interesting electronic and optical properties for which they find suitable applications in ceramic pigments.[29-32] The main limitation of these aluminates in pigment application is their chemical reactivity at higher temperatures which can be subdued by using inert aluminosilicate (mullite) as encapsulant.[27]

During the course of our work nanocrystalline mullite phases have been synthesized via sol-gel route from a non-stoichiometric precursor with x=0.29 (61.54 mol% alumina) which corresponds to a little high alumina content in the mullite species. With increasing alumina content a greater number of oxygen vacancies are formed in the mullite structure to maintain charge neutrality due to which silicon deficient mullite leads to some interesting mechanical, electrical and photoluminescence properties. Thus, the effect of transition metal ions (Co^{2+}, Ni^{2+} and Cu^{2+}) on different physico-chemical properties of mullite and their effect on mechanical strength, dielectric and photoluminescence properties were studied in this paper.

View Article Online
DOI: 10.1039/C5RA21091G

2. Experimental:

2.1. Materials:

All reagents used in this synthesis procedure are of analytical grade and >99% pure. The chemicals used in this preparation are aluminium isopropoxide ($Al(O\text{-}i\text{-}Pr)_3$)(AIP) (Loba Chemie, Mumbai, India), tetraethoxysilane (TEOS) ($Si(OC_2H_5)_4$) (Merck, Honenbrunn, Germany), absolute ethanol (Merck, Worli, Mumbai, India), cobalt chloride hexahydrate ($CoCl_2.6H_2O$) (Merck, Worli, Mumbai, India), nickel chloride hexahydrate ($NiCl_2.6H_2O$) (Merck, Worli, Mumbai, India), copper chloride hexahydrate ($CuCl_2.6H_2O$) (Merck, Worli, Mumbai, India).

2.2. Sol-gel synthesis of nanocrystalline mullite from non-stoichiometric precursors :

A sol-gel synthesis of non-stoichiometric mullite precursor (61.54 mol% alumina and mole ratio of Al/Si was 3.2) was performed using aluminium isopropoxide (AIP) and tetraethoxysilane (TEOS) as source of alumina and silica respectively (Figure 1).

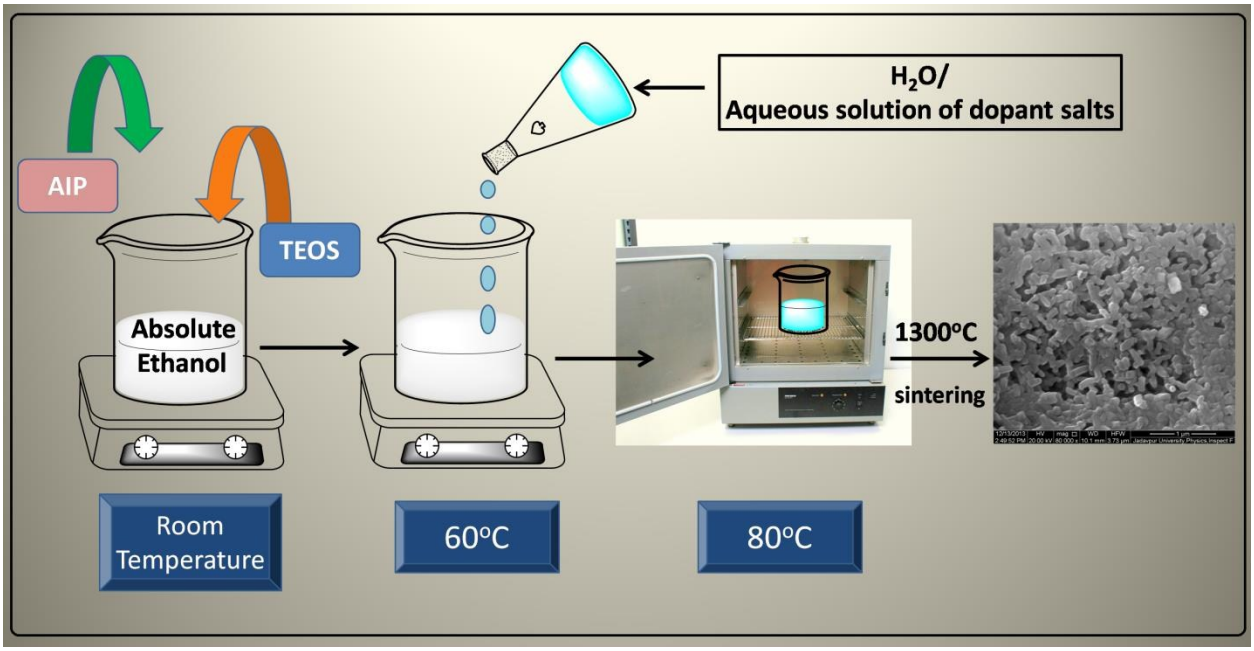

Figure 1: A schematic diagram for the preparation of transition metal ions conjugated mullite nanocomposites

The composition of the aluminosilicate precursor was kept slightly in the alumina rich zone intentionally to minimize glassy formation during sintering. Initially, AIP and TEOS with mass ratio 3.15 were simultaneously added to absolute ethanol and magnetically stirred overnight for the formation of precursor sol. Alkoxide solution was then hydrolysed by adding of 20 ml of deionized water to form precursor sol under stirring at a fixed temperature of 60°C. Precursors with dopant transition metal ions were prepared by the addition of 20 ml aqueous solution of cobalt chloride hexahydrate, nickel chloride hexahydrate and copper chloride dehydrate to the

View Article Online
DOI: 10.1039/C5RA21091G

alkoxide solution during the hydrolysis step so that the resulting molarity of metal ions in the precursor volume was 0.03(M), 0.06(M), 0.14(M) and 0.23(M) respectively. The pure and doped mullite gels obtained via hydrolysis of sol were dried at 80^{o}C in a hot air oven and the dried gel was sintered at 1300^{o}C in a muffle furnace under air atmosphere with heating rate of 600^{o}C/h and 2 h soaking to obtain transition metal ions conjugated mullite nanocomposites for further characterization. The designations of pure and doped mullite composite samples have been given in table 1.

Molarity of dopant salt solution	**Final molarity in resulting precursor volume**	**Co^{2+} doped mullite precursors**	**Ni^{2+} doped mullite precursors**	**Cu^{2+} doped mullite precursors**
0	0	M_{00}	M_{00}	M_{00}
0.1	0.03	M_{11}	M_{21}	M_{31}
0.2	0.06	M_{12}	M_{22}	M_{32}
0.5	0.14	M_{13}	M_{23}	M_{33}
0.8	0.23	M_{14}	M_{24}	M_{34}

Table 1: Description of prepared samples along with their designations

2.3. Characterizations:

Crystallization, phase formation and microstructural analysis of pure and transition metal ions doped mullite were performed by X-ray diffraction (XRD) (Bruker AXS INC., Madison, WI), Fourier Transform Infrared Spectroscopy (FTIR – 8400S, Shimadzu) and FESEM (INSPECT F50, Netherland).

The phase formation of mullite and mullite composite was studied by the X-ray diffraction using Cu Kα radiation – 1.5409Å, 2θ=10^{o} – 70^{o}, scan speed 0.1 sec/step, increment – 0.02, operating voltage – 40 KV, and operating current – 40 mA.

FTIR spectroscopic studies of mullite powders sintered at different temperatures were done by KBr pellet method between the wavenumbers 500 cm^{-1} to 1500 cm^{-1}.

The field emission scanning electron micrographs of the samples were taken after being coated with gold via plasma spraying at 0.1 millibar pressure. The samples were kept inside vacuum chamber with pressure about $5x10^{-3}$ Pa at distance15 mm away from the detector with spot size 3.0 mm. The emission current and operating voltage were kept at 170 µA and 20 KV respectively.

Archimedes' principle was used to measure the relative density of all samples using xylene as buoyant medium. The absolute density of the samples was determined employing the relation:

View Article Online
DOI: 10.1039/C5RA21091G

$$\rho = \frac{W_a}{W_a - W_b} \times \rho_b \quad \ldots\ldots\ldots (1)$$

where W_a is weight of the sample in air, W_b is the weight of the sample in the buoyant medium, ρ is the density of the sample and ρ_b is the density of the buoyant liquid (0.86 g/cc at 25°C for Xylene). Assuming theoretical density of mullite, cobalt oxide, nickel oxide and copper oxide as 3.16 g/cc, 6.11 g/cc, 6.67 g/cc and 6.31 g/cc, the relative density $\left(\frac{Calculated\ density}{Theoritical\ density}\right) \times 100\ \%$ and apparent porosity of the samples were measured.

Vickers (H_V) and Knoop Hardness (H_K) of the polished sample pellets were measured using Leco's hardness tester which contains a nanoindenter (Leco, LV700). In case of Vickers hardness test the indenter is a square based pyramid with angle (ψ) between the two opposite sides being 136° whereas for Knoop indenter a lozenge-based pyramid was used with angle (θ) between two opposite faces being 172°5′ and the angle (φ) between the other two being 130°. Hardness of a material is described as the ratio between the indentation load and parameter representing area of residual impression which depends on the shape of the indenter. Ten impressions have been made on the surface of the samples using load of 1kgf during ten seconds. After removal of the indenter, by measuring the dimension of indentations via an optical microscope with 20x zooming, the Vickers and Knoop hardess number of the composite were calculated according to the following equations:

$$H_V = \frac{P}{A_{TAC}} = \frac{P}{\frac{d^2}{2}\sin\frac{\psi}{2}} = 1.8544\ \frac{P}{d^2} \quad \ldots\ldots\ldots (2)$$

$$H_K = \frac{P}{A_{PAC}} = \frac{P}{L^2\frac{\tan\varphi/2}{2\tan\theta/2}} = 14.299\ \frac{P}{L^2} \quad \ldots\ldots\ldots (3)$$

Where H_V and H_K are Vickers and Knoop hardness numbers respectively expressed in MPa, P is the applied load in N, d is the indentation diagonal for Vickers and L is the longer indentation diagonal for Knoop indentation in mm, A_{TAC} represents the true area of contact and A_{PAC} represents projected area of contact for Vickers and Knoop indentation respectively.[33]

The dielectric properties of the composite were investigated by measuring the frequency dependent capacitance and tangent losses using a digital LCR meter (Agilent, E4980A) with circular Ag electrodes under room temperature and pressure with 1 V applied signal and frequency ranging between 20 Hz to 2 MHz. The dielectric constant (ε) and the ac conductivity (σ_{ac}) of the pure and doped mullite composite were calculated according to the following equations respectively,

$$\epsilon = \frac{C.d}{\varepsilon_0.A} \quad \ldots\ldots\ldots (4)$$

View Article Online
DOI: 10.1039/C5RA21091G

$$\sigma_{ac} = 2\pi f \varepsilon \varepsilon_0 \tan\delta \quad \ldots\ldots\ldots (5)$$

where, *C*, *d*, *A* and *tan* δ are the capacitance, thickness, area and tangent loss of the samples respectively, *f* is the frequency of applied ac voltage in Hz and ε_0 is the absolute permittivity of free space with value 8.854 x 10^{-12} F/m.

The photoluminescence of the composite was measured Cary Eclipse fluorescence spectrophotometer, Agilent Technologies taking 0.1 mg/mL solution of the samples in absolute ethanol medium. The fluorescence microscopic images of selected samples were taken under Zeisss Axiocam MRc with 50x zooming.

3. Results and Discussions:

3.1. X-ray diffraction analysis:

The comparative powder X-ray powder diffraction data of pure and Co (II), Ni (II) and Cu (II) ion incorporated mullite composites have been shown in Figure 2.

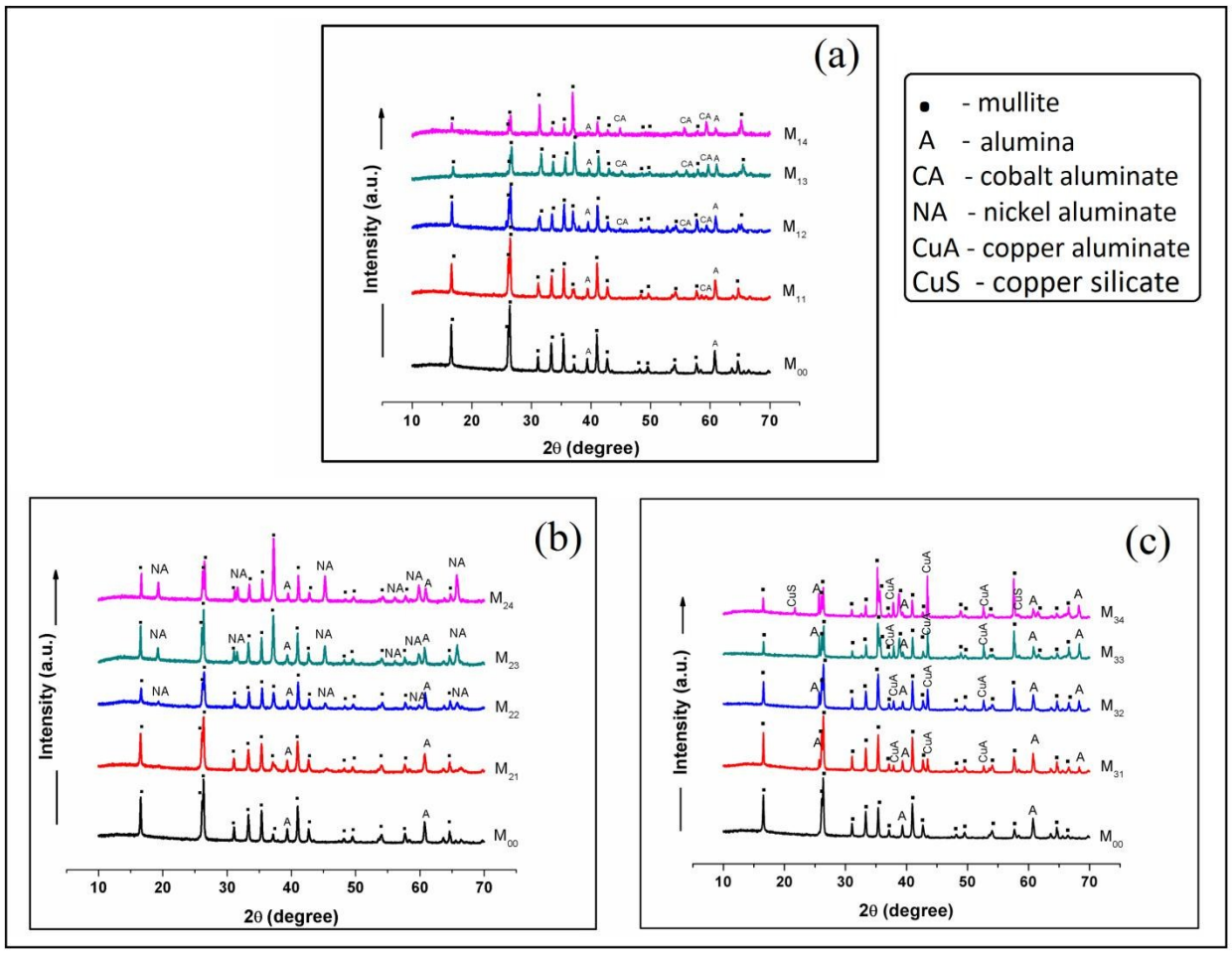

Figure 2: A comparative powder X-ray diffraction pattern of pure and (a) Co^{2+}, (b) Ni^{2+} and (c) Cu^{2+} doped mullite nanocomposite sintered at 1300ºC.

View Article Online
DOI: 10.1039/C5RA21091G

Well crystalline mullite phase is reflected in the diffraction pattern along with reflections of alumina for both pure and doped mullite composites. For 0.03 (M) solution of all dopant transition metals, very little change in mullitization occurred that was confirmed by small difference between heights of characteristic mullite peaks compared to the pure mullite. In comparison to other metal ions the difference in peak heights for 0.03 (M) nickel chloride doping (Figure 2b) was much lower which is indicative of better mullitization for nickel ion doping. This is due to higher extent of interaction of Ni^{2+} with aluminosilicate matrix. Co^{2+}, Ni^{2+} and Cu^{2+} ions due to their lower valency and larger ionic radius cannot be readily incorporated into mullite structure but their oxides have been found to form Co, Ni and Cu aluminates (spinel phases) due to solid state diffusion of these oxides within alumina. The spinel formation rate follows the sequence $CuAl_2O_4$> $CoAl_2O_4$> $NiAl_2O_4$ which depends on the diffusivity of metal ions towards AlO_6 octahedron.[30] Increasing concentration of transition metals has a detrimental effect on mullitization since alumina is consumed to form spinel phases (aluminate phases) at higher doping concentration of metal ions resulting in a lower dissolution rate of Al_2O_3 into molten SiO_2 flux. The intensity of the peaks corresponding to crystalline alumina that are reflected in the diffractogram of doped mullite composites, decreased significantly as the aluminate phases were found to grow from respective oxides at higher doping. In case of cobalt and copper ion, spinel phases arrived from 0.03 (M) salt concentration (Figures 2a and 2c) and grew distinctly at higher doping concentration whereas for nickel ion doping, reflections corresponding to nickel aluminate phase started to grow at 0.06 (M) nickel chloride concentration (Figure 2b) due to low spinel forming capability of nickel ion. In air atmosphere, Co^{2+}, Ni^{2+} and Cu^{2+} from their respective salts, form CoO, NiO and CuO at high temperature sintering followed by the formation of aluminate phases from these oxides upon reacting with alumina. At higher temperature, around 1050^{o}C CuO (Cu(II)) may transform into Cu_2O (Cu(I)) which also contribute to the formation of aluminate phases besides Cu(II).[34] Due to higher diffusivity of Cu^+ during incubation period at 1300^{o}C, copper silicate phases along with aluminate phases were also observed in the X-ray diffraction pattern (Figure 2c) when salt concentration reaches 0.23 (M), which indicates that Cu^+ reacted not only with AlO_6 octahedron but also with SiO_4 tetrahedron. On the other hand, owing to lower diffusivity of Co(II) and Ni(II) as compared to Cu(I), they react only with AlO_6 octahedra and not with the SiO_4 tetrahedron.

The average particle size was calculated from Debye-Scherrer's equation which is as follows: $D = \frac{0.9\lambda}{\beta cos\theta}$ where D is average particle diameter, λ is wavelength of Cu Kα radiation, β is full width of half maxima in radian for the characteristic mullite peak at $2\theta=16^o$ (where θ is Bragg's angle) corresponding to (110) plane. The dimensions of the particles as calculated from Debye Scherrer's equation are in nanometer regime for pure and transition metal mullite composite (Table 2).

View Article Online
DOI: 10.1039/C5RA21091G

Sample	Average Particle size (nm) (from XRD)	Bulk Density (%)	Apparent porosity (%)	Dielectric constant At 1 KHz	Vicker's Hardness (GPa)	Knoop Hardness (GPa)	Young's modulus (GPa)
M_{00}	46	62.59	37.41	91.3	1.6	1.7	46.7
M_{11}	43	66.77	33.23	98.1	3.5	3.6	76.5
M_{12}	48	80.84	19.16	73.1	5.2	5.6	135.7
M_{13}	51	83.47	16.53	80.2	5.9	6.3	153.6
M_{14}	59	84.88	15.12	68.2	6.9	7.5	207.3
M_{21}	43	81.09	18.91	108.6	2.6	2.7	63.3
M_{22}	43	82.1	17.9	175.3	5.4	5.8	142.4
M_{23}	55	96.23	3.77	64.7	5.9	6.2	153.2
M_{24}	57	98.89	1.11	67.7	6.5	6.9	167.2
M_{31}	58	64.56	35.44	50.1	3.3	3.4	72.2
M_{32}	52	74.9	25.1	56.3	6.8	7.1	170.5
M_{33}	65	76.24	23.76	77.2	7.5	7.8	177.2
M_{34}	56	82.91	17.09	64.9	8.7	8.7	174.6

Table 2: Particle size from Debye-Scherrer's equation, relative density, apparent porosity, dielectric constant, hardness and Young's modulus for pure and transition metal ions doped mullite composites.

3.2. FTIR analysis:

FTIR spectra of Co^{2+}, Ni^{2+} and Cu^{2+} doped mullite composites have been given in Figure 3.

View Article Online
DOI: 10.1039/C5RA21091G

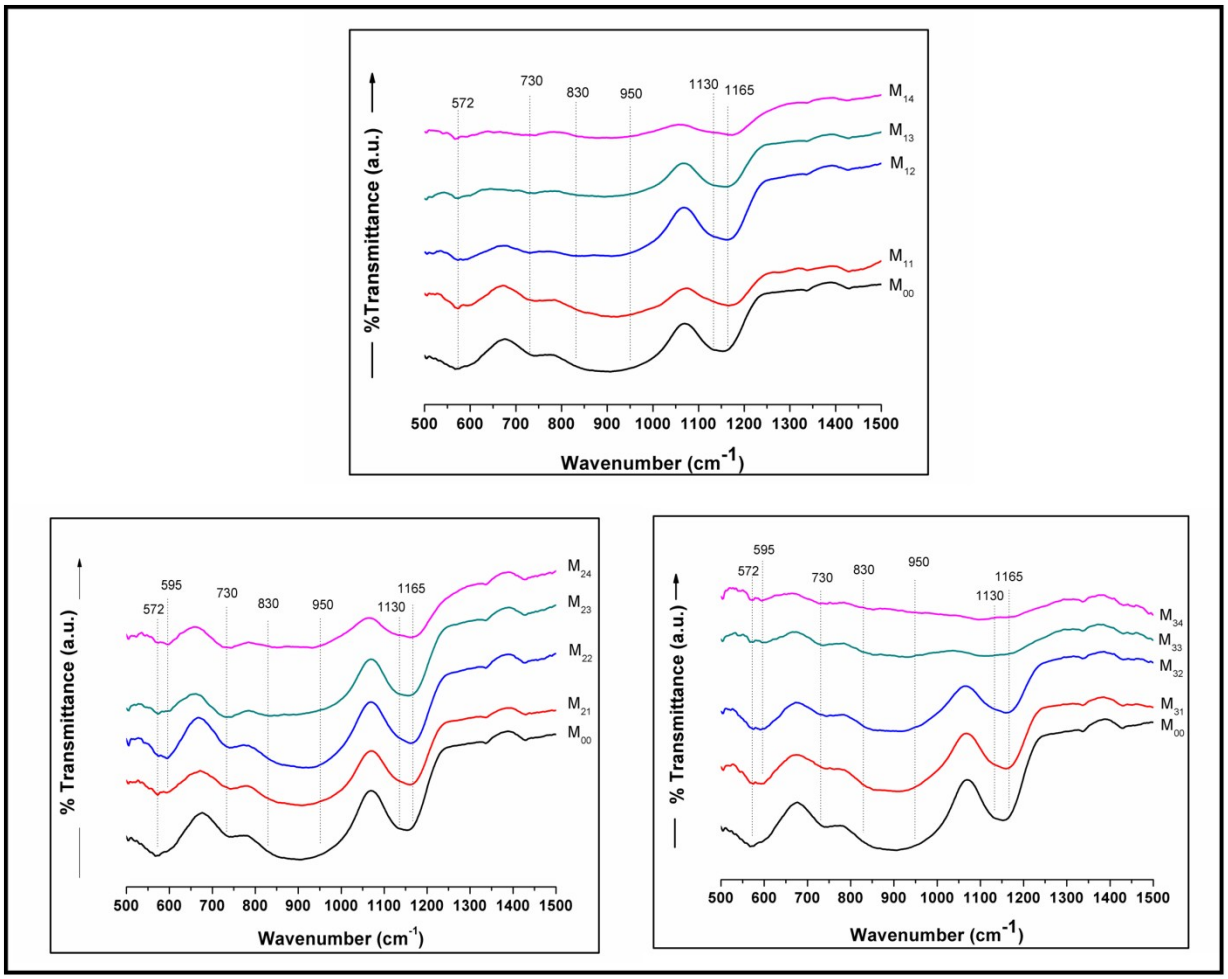

Figure 3: Fourier transform infrared spectra of pure and (a) Co^{2+}, (b) Ni^{2+} and (c) Cu^{2+} doped mullite nanocomposites sintered at 1300ºC.

Characteristic bands of mullite were reflected at wavenumbers 572 (octahedral Al-O stretch), 730 (tetrahedral Al or Si bend), 830 (tetrahedral Al-O stretch), 950 (Si-O stretch), 1130 (tetrahedral SiO_4 stretch) and 1165 cm^{-1}(Si-O stretch) for pure and transition metal ion doped mullite samples.[8, 35-36] In case of Ni^{2+} and Cu^{2+} doping, additional peak for Al-O stretching vibration were obtained at 595 cm^{-1} (Figures 3b and 3c). Reflections of octahedral and tetrahedral Al-O stretching vibrations, tetahedral Si-O stretching in the FTIR spectra is indicative of the presence of mullite in the composites whereas the detrimental transmission intensity of Al-O stretching vibrations due to transition metal ion doping clearly reflects the consumption of alumina towards the formation of spinel phases.

3.3. FESEM analysis:

Microstructures of mullite and transition metal ions conjugated mullite composites have been shown in Figure 4.

View Article Online
DOI: 10.1039/C5RA21091G

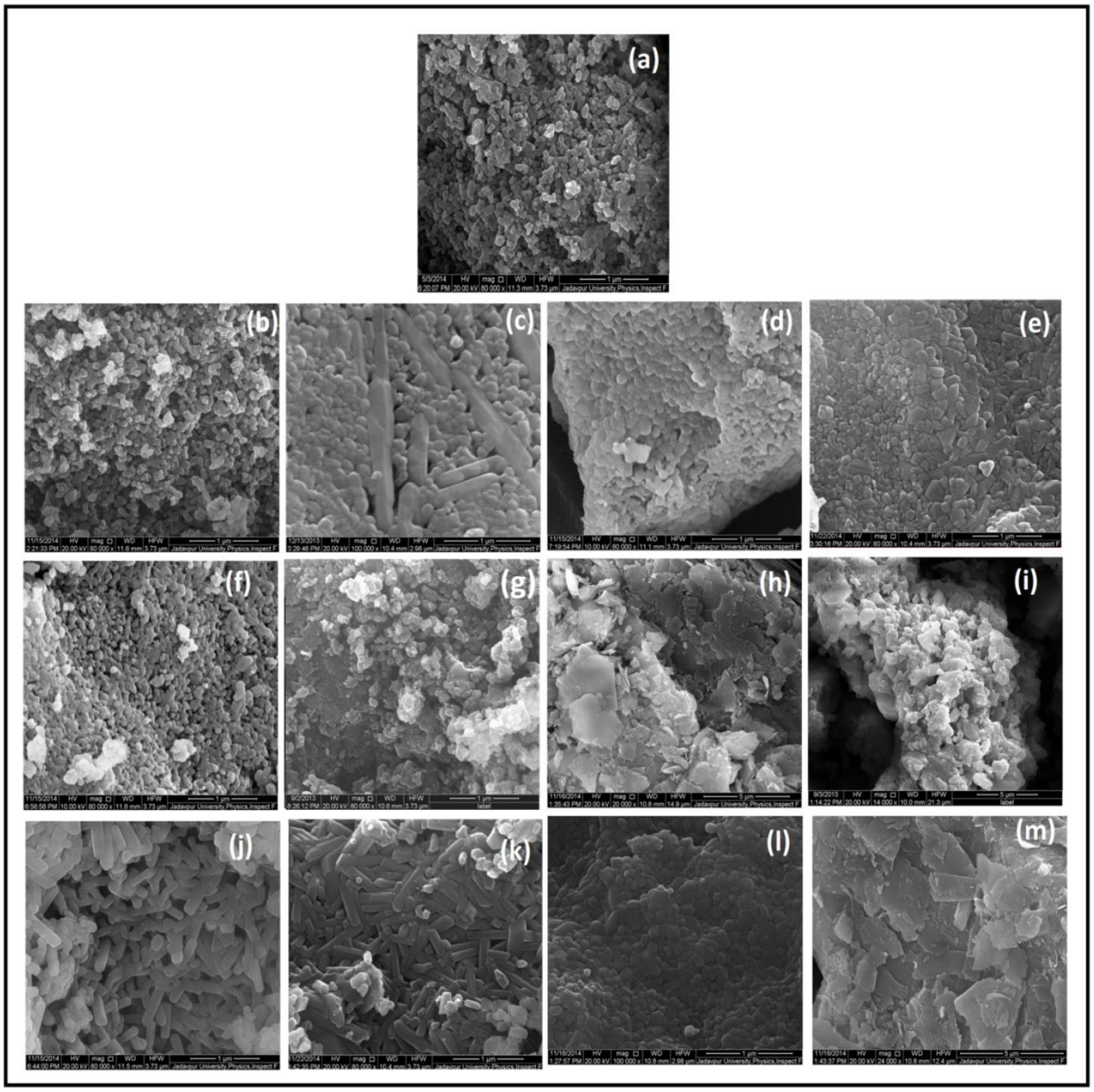

Figure 4: Field emission scanning electron micrographs of (a) pure mullite (M_{00}), cobalt doped mullite (b) M_{11}, (c) M_{12}, (d) M_{13} and (e) M_{14}, nickel doped mullite (f) M_{21}, (g) M_{22}, (h) M_{23} and (i) M_{24} and copper doped mullite (j) M_{31}, (k) M_{32}, (l) M_{33} and (m) M_{34}.

The nanometer dimension of equiaxed mullite grains was obvious from the FESEM micrograph (Figure 4a) of pure mullite with average particle diameter ~100 nm along with clearly visble porosity. The micrographs of cobalt and nickel ion doped mullite with lowest doping concentration (Figures 4b and 4f) are similar to that of pure mullite with increased grain size which indicates no significant morphological changes to mullite structure due to these doping. Non-uniform microstructure with equiaxed grains distributed among abnormal elongated grains was observed for 0.06 (M) doping concentration of cobalt chloride salt which reflects abnormal

View Article Online
DOI: 10.1039/C5RA21091G

grain growth of mullite.[37] Improved microstructures were observed for much higher cobalt ion concentration with some elongated grains of average width ~ 120-160 nm distributed among equiaxed grains of average diameter ~100-150 nm that identify the biphasic nature of the precursor gels. In case of dopant nickel ion, no drastic morphological changes are visible upto 0.06 (M) doping concentration whereas in case of 0.14 (M) and 0.23 (M) doping concentration, conglomerated sheet like and concoid structure of nickel aluminate were reflected respectively in the micrographs (Figures 4h and 4i). Elongated grains of average width ~100 nm decorated with smaller mullite grains of average diameter ~80 nm were obtained (Figures j-k) for 0.03 and 0.06 (M) doping concentration of copper chloride solution whereas for 0.14 (M) concentration some small copper aluminate grains (Figure 4l) were also observed along with mullite grains. In case of highest doping with copper ion, sheet like structures (Figure 4m) of copper aluminate were formed. No Alumina structures and no metal aluminate structures at lower doping concentrations of the dopant solutions were spotted due to their lower extent of formation. The increase in grain size and densification behavior for higher doping concentration in all the composite were also reflected in the FESEM microstructures.

3.4. Densification Behavior:

Densification behavior of transition metal-mullite nanocomposites have been shown in Figure 5.

View Article Online
DOI: 10.1039/C5RA21091G

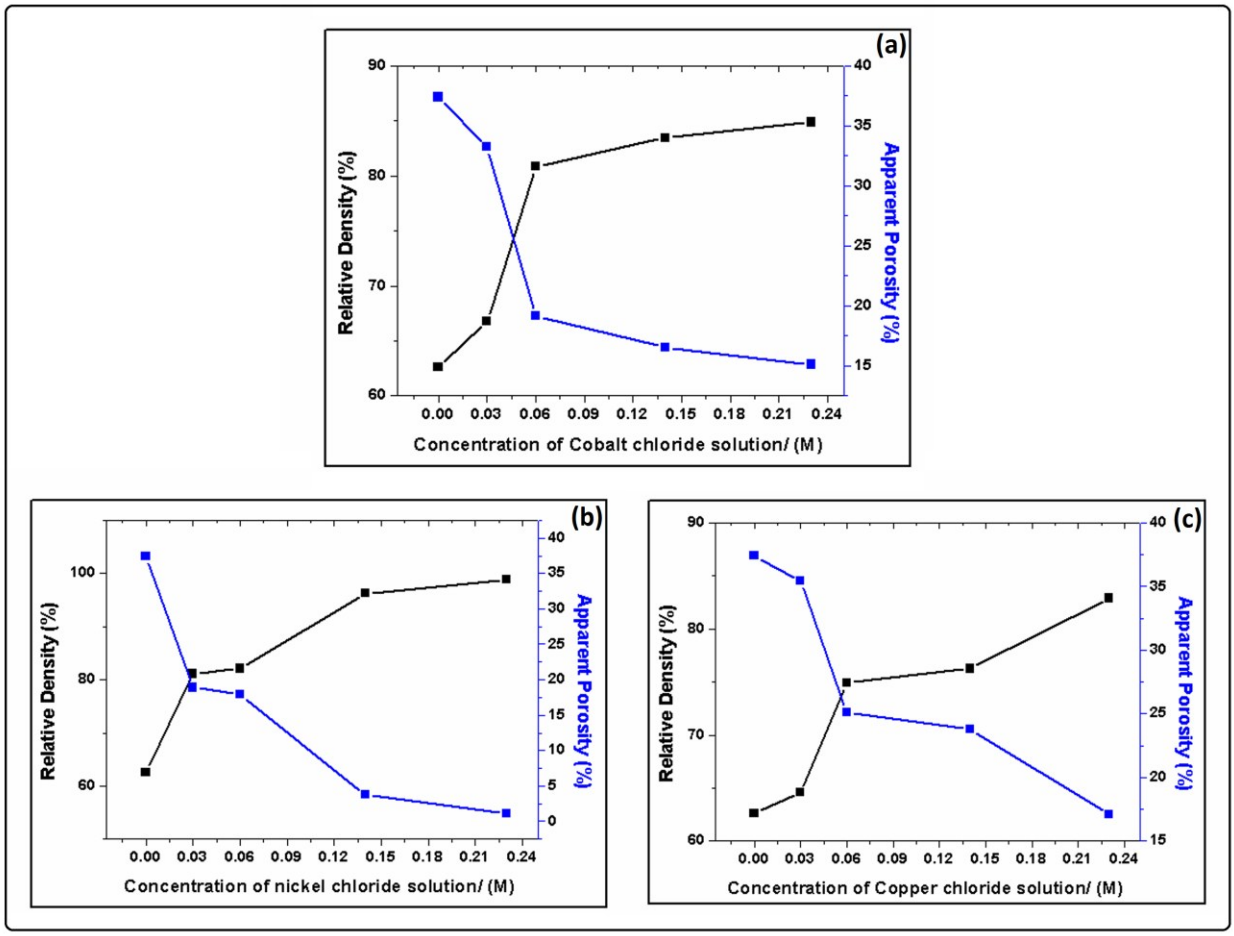

Figure 5: Densification behavior and variation of apparent porosity of mullite doped with (a) Co^{2+}, (b) Ni^{2+} and (c) Cu^{2+}.

The highly porous nature (~37% apparent porosity) was evident in undoped mullite system due to higher gelation rate, higher evaporation rate of alcohol solvent and lower phase segregation. In case of all dopant transition metal ions, the relative density of the doped mullite composites increased with higher extent of doping accompanied by a gradual decrease in apparent porosity. The highest relative density of ~ 99% was obtained for the mullite sample doped with 0.23 (M) dopant solution of nickel chloride and for highest doping concentration of Cobalt and copper solution, the same was found to be ~85 and ~83% respectively (Table 2). This higher relative density along with dwindling apparent porosity may be caused due to increased consolidation at 1300^{o}C, formation of interstitial aluminate phases in trasition metal ions doped mullite composite, higher cation mobility due to formation of cation vacancy resulting from the substitution of Al^{3+} by transition metal ions and finally due to higher rate of body diffusion for the contribution of liquid phases by transition metal ions in terms of their corresponding oxides.[38, 39]

View Article Online
DOI: 10.1039/C5RA21091G

3.5. Color of the transition metal mullite composites:

Formation of transition metal complexes by Co, Ni and Cu due to the incorporation of oxygen results in a shift of the absorption band towards visible region (wavelength between 400 to 800 nm) of the electromagnetic spectrum and thus accounts for a wide range of applications as ceramic pigments. $CoAl_2O_4$, $NiAl_2O_4$ and $CuAl_2O_4$ due to their interesting physical and chemical properties including their excellent colours are being used in industries as ceramic pigments.[27] The formation of these aluminates from transition metal ions doped mullite precursors after sintering at 1300^oC introduced sustainable color in the samples which make these mullite based transition metal aluminates suitable for pigment applications.[26] No absorption in the visible region occurred for pure mullite samples which results in white color of the pellet whereas deep blue, pale blue and brown colour appeared for Co, Ni and Cu doped mullite composites respectively due to formation of $CoAl_2O_4$, $NiAl_2O_4$ and $CuAl_2O_4$ (Figure 6).

View Article Online
DOI: 10.1039/C5RA21091G

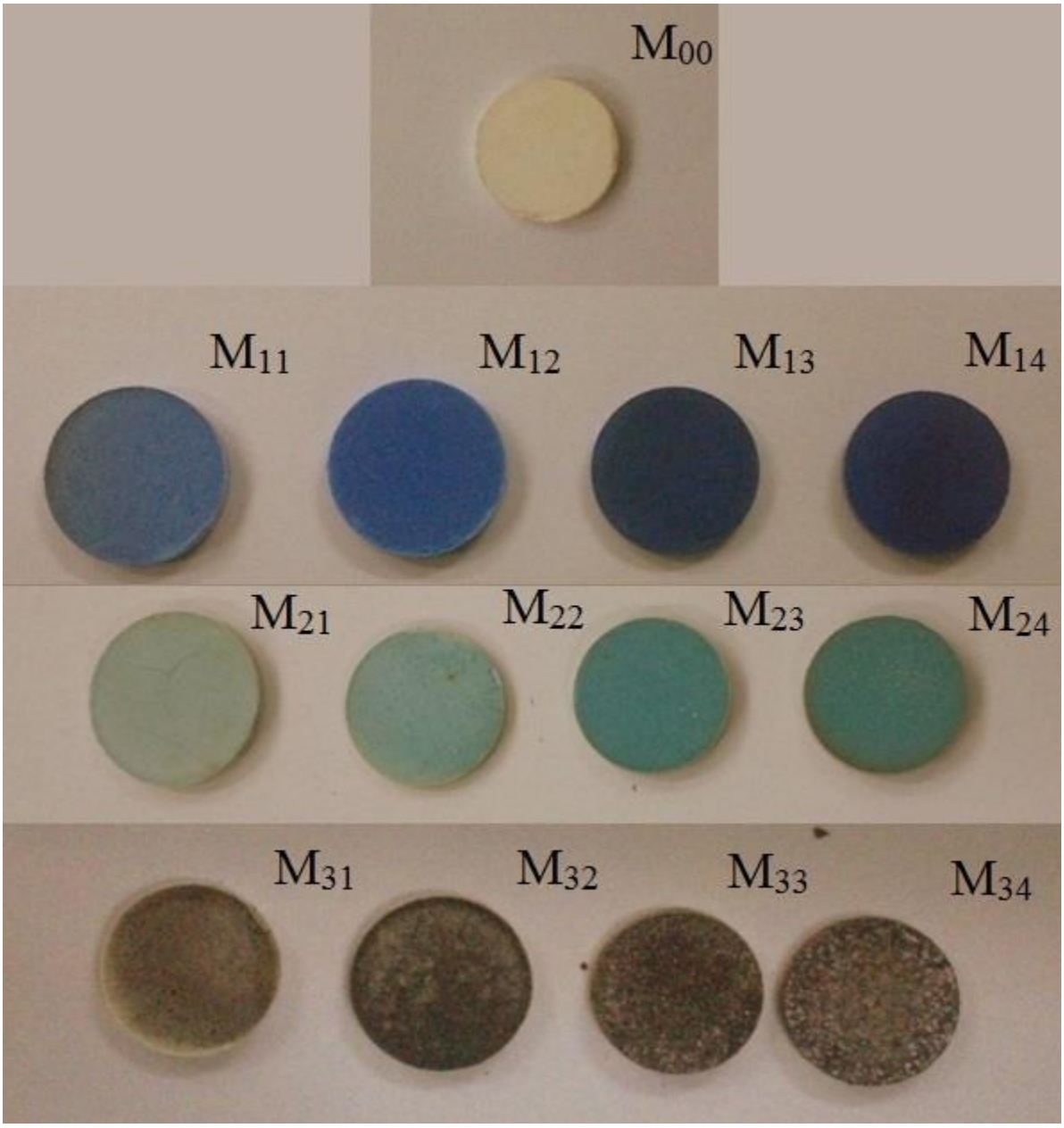

Figure 6: Digital images for the pellets of pure and transition metal ions conjugated mullite composites after sintering at 1300°C.

The appearance of the color was found to be intensified for increasing doping concentration of all three transition metal ions which may be due to the enhanced formation of aluminate phases.

3.6. Mechanical Properties:

3.6.1. Comparison between Vickers and Knoop hardness:

To compare between Vickers and Knoop hardness values, 9.8 N stresses was applied on the polished specimen surfaces of all samples during 10 seconds in order to ignore indenter size effect. The difference between the hardness values for differently shaped Vickers and Knoop

View Article Online
DOI: 10.1039/C5RA21091G

indenters may be caused due to the different extent of elastic recovery resulting from mismatch between the plastic zone beneath the indentation and the surrounding elastic deformed region after removal of the indenters.[33] Lawn and Howes[40] proposed that change in the indentation diagonal length was negligible for Vickers indentation though elastic recovery occurs along the depth of the indentation whereas for Knoop indentation Marshall et al.[41] observed that length of the minor diagonal is often less than the theoretical one calculated via geometric consideration of the indenter which is attributed to elastic recovery of the material. Ratio of short (s) and long indentation diagonal lengths (L) of Knoop impression was expressed as a function of the ratio between Knoop hardness (H_K) and Young's modulus (Y) by Marshall et al. according to following equation.

$$\left(\frac{s}{L}\right)_{measured} = \left(\frac{s}{L}\right)_{theoritical} - 0.45\left(\frac{H_K}{Y}\right) \dots\dots\dots (6)$$

On the other hand, Gong et al.[42] explained that two hardness values differing in magnitude is indicative of a difference between degree of elastic recovery in both cases neglecting different plastic zones for the indenters. They further determined a correlation between s/L and the hardness ratio H_V/H_K according to the following equation

$$\left(\frac{s}{L}\right)_{measured} = 0.1908 - 0.0595\left(\frac{H_V}{H_K}\right) \dots\dots\dots (7)$$

Later, Chicot et al.[33] showed that the equation (7) given by Gong et al. is not valid for all range of hardness values. Equation (7) is not valid for 0-7.9 GPa hardness values since in this range, according to Chicot et al. the Vickers hardness value (H_V) is less than the Knoop hardness value (H_K) which make the measured value of s/L higher than the theoretical one (0.1406). Due to elastic recovery, the shortening of the minor diagonal of Knoop indentation and hence lowering of s/L value are obvious after removal of the indenter and thus experimental value of s/L must be less than the theoretical value of s/L which equals to 0.1406 as calculated from geometric point of view. In this context the higher value of measured s/L after removal of Knoop indenter compared to the theoretical one has no physical significance since it corresponds to elastic collapse. To remove this ambiguity, Chicot et al. modified the equations (6) and (7) to be applicable for all range of hardness values. They suggested that Vickers and Knoop hardness values should be calculated in the same scenario for which they consider true area of contact instead of projected area of contact for Knoop hardness measurement to relate it with Vickers hardness measurement from equation (2). In order to recalculate the Knoop hardnes value using true area of contact Chicot et al. suggested an equation which is nothing but a modified form of equation (3) and given as follows:

$$(H_K)_{TAC} = \frac{P}{A_{TAC}} = 12.873\frac{P}{L^2} \dots\dots\dots (8)$$

Equation (8) and (3) are almost similar only differing in numerical constant (14.299 in equation (3) and 12.873 in equation (8)) for which it can be written from these to equations that

$$(H_K)_{TAC} = \frac{12.873}{14.299}H_K = 0.9047\ H_K \dots\dots\dots (9)$$

View Article Online
DOI: 10.1039/C5RA21091G

Chicot et al. also suggested to modify equations (6) and (7) correctly according to the following two:

$$\left(\frac{s}{L}\right)_{measured} = \left(\frac{s}{L}\right)_{theoritical} - 0.5\left(\frac{H_K}{Y}\right) \ldots\ldots\ldots (10)$$

and

$$\left(\frac{s}{L}\right)_{measured} = 0.1908 - 0.0658\left(\frac{H_V}{H_K}\right) \ldots\ldots\ldots (11)$$

During the course of our work we followed Chicot et al.'s formalism since all the values of hardness for all samples except copper ion doped mullite at its highest doping concentration falls below the critical hardness value of 7.9 GPa (Table 2). All hardness data was in agreement with the generalization of hardness and thus Vickers hardness is obtained to be less than that of Knoop hardness value for less than 7.9 GPa hardness. In case of 0.23 (M) dopant copper solution, both the hardness values was found to be 8.7 GPa which may attributes to the fact that this hardness value not ranging too far from the critical value (7.9 GPa) of hardness, difference between the two hardness values is not very prominent. Plots between $(H_K)_{TAC}$ and H_V as well as between s/L and $H_V/(H_K)_{TAC}$ have been shown separately for different metal ion doping (Figures 7a and 7b).

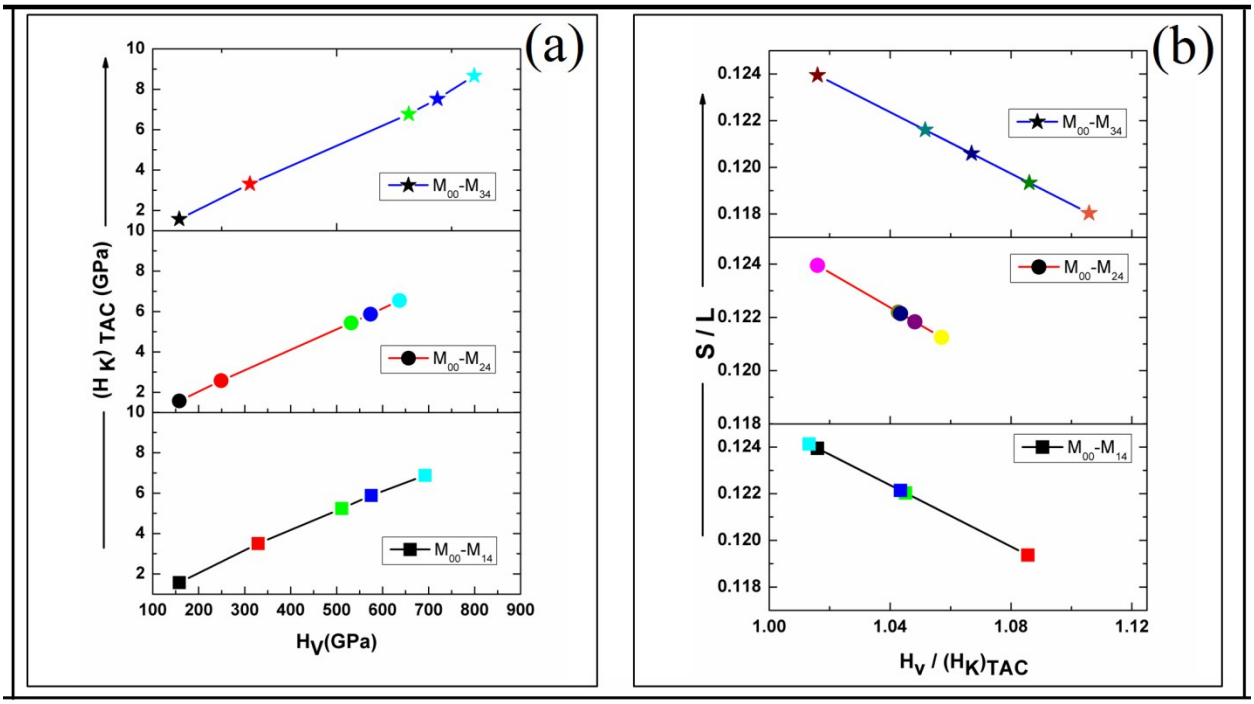

Figure 7: Plots of (a) $(H_K)_{TAC}$ v/s H_V and (b) s/L v/s $H_V/(H_K)_{TAC}$

Both the plots show a straight line nature only differing in slope (positive slope for $(H_K)_{TAC}$ v/s H_V plot and negative slope for s/L v/s $H_V/(H_K)_{TAC}$ plot) and this straight line nature of the graphs is in agreement with Chicot et al. and suggests their modified equations to be valid for mullite ceramics and mullite matrix composites too. Young's modulus of pure mullite and transition

View Article Online
DOI: 10.1039/C5RA21091G

metal ion mullite composite were calculated from equation (10) and its variation was discussed in the following section.

3.6.2. Doping concentration dependent mechanical properties:

Figure 8a shows the variation of Vickers and Knoop hardness with increasing doping concentration of transition metal ions.

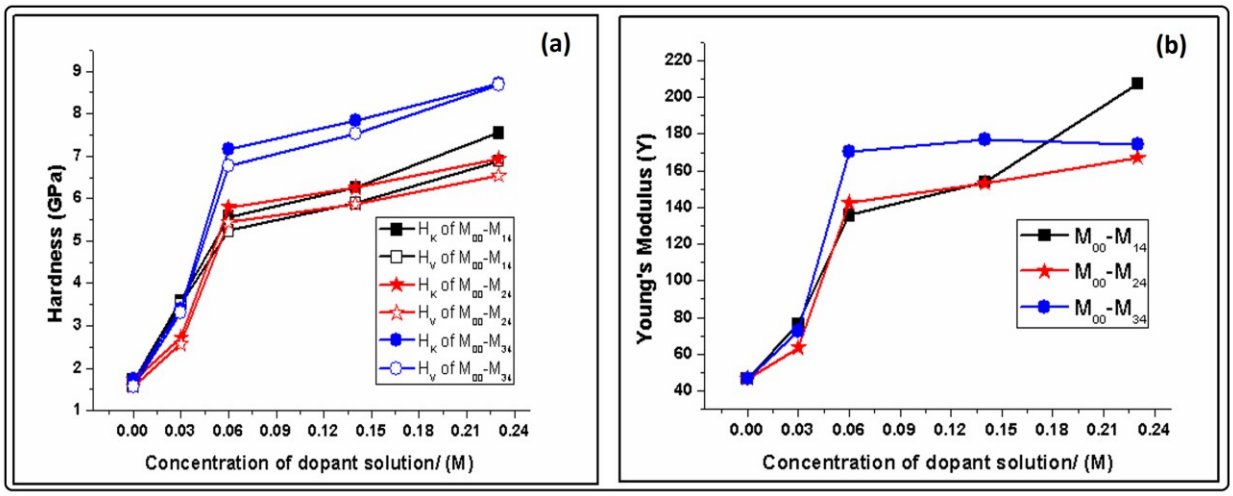

Figure 8: Variation of (a) hardness and (b) Young's modulus with doping concentration of transition metal ions

The Vickers and Knoop hardness of pure mullite was found to be 1.6 and 1.7 GPa respectively which may be due to the higher resulting porosity of pure mullite (Table 2). The increase in both Vickers and Knoop hardness values with increasing doping concentration of transition metal ions were observed and highest value (~ 8.7 GPa) for both the hardness were obtained in case of 0.23 (M) copper chloride solution (Table 2) which is higher than other mullite composite as reported in literatures.[4, 24, 43] The higher densification, larger grain size and the formation of dislocation networks in matrix grains as well as strengthed grain boundaries are responsible for higher mechanical strength of composites.[44] Among several strengthening mechanisms chiefly grain boundary strengthening are responsible for the enhanced strength of the transition metal ions doped mullite composites. Mechanical properties of materials can be enhanced by prohibiting the dislocation motions in the grains. The transition metal ions cause lattice distortions in mullite that hinder dislocation motion which results in higher mechanical strength of mullite upon doping with transition metals. Grain size has a significant influence on the mechanical properties of polycrystalline materials. Due to different crystallographic orientations of grains, grain boundaries arise which act as an impediment to dislocation motions in the grains because lattice structure of adjacent grains being different in crystallographic orientations, more energy is required for a dislocation to change its direction and move to neighboring grain. Smaller grain size and interstitial formation of aluminate phases for transition metal ions doping introduce large number of grain boundaries which oppose dislocation motions resulting in higher

View Article Online
DOI: 10.1039/C5RA21091G

values of hardness.[20] Variation of Young's modulus with doping concentration of dopant transition metal salts are shown in Figure 8b. Due to nanometer dimensions of mullite and spinel grains, increase in Young's modulus of the mullite composite with higher doping with transition metal ions can be explained by inverse Hall Petch effect. According to this effect, yield strength increases with increasing grain size which signifies higher extent of elasticity of the material resulting in higher Young's modulus. The small decrease in the value of Young's modulus for 0.23 (M) doping concentration of copper chloride may be caused due to the formation of copper silicate phases (Figure 8b).

3.7. Dielectric behavior:

3.7.1. : Doping concentration dependent dielectric properties for different transition metal ions:

Figure 9 shows the variation of dielectric constants and tangent losses at 1 KHz frequency for cobalt, nickel and copper ion doped mullite composites.

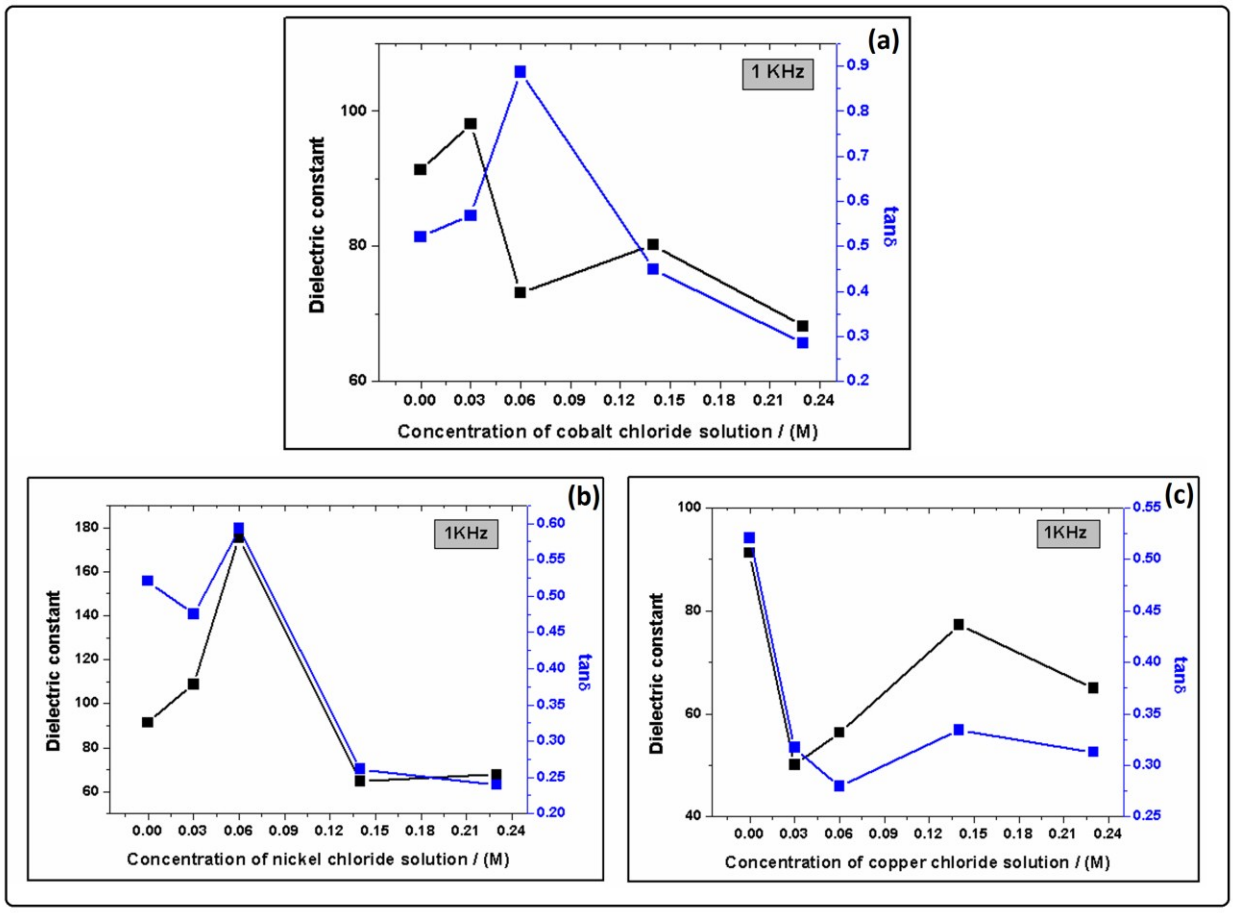

Figure 9: Doping concentration dependent dielectric constant and tangent losses of mullite composite doped with (a) Co^{2+}, (b) Ni^{2+} and (c) Cu^{2+} at 1 KHz frequency.

View Article Online
DOI: 10.1039/C5RA21091G

Highest dielectric constant (~ 175) was obtained in case of nickel doping at its highest concentration of doping (M_{24}) (Table 2) which may be explained in terms of Jahn-Teller distortion. The unpaired electron in the t_{2g} orbital of Co^{2+} (d^7 electron system) and three electrons in two degenerate e_g orbitals of Cu^{2+} (d^9 electron system) lead to Jahn teller distortion in mullite composite gel matrix which in turns lower the energy.[13, 16] However, Ni^{2+} due to its symmetrically filled e_g orbitals and t_{2g} orbital show no distortion in precursor gel for which the energy of nickel ion doped mullite composite should be greater than that of cobalt and copper doped mullite composites.[16] This higher energy of nickel ion doped mullite composites promotes higher entropy of the induced dipoles upon the application of external electric field resulting in higher dielectric constant. Moreover, it is obvious that in electronic and ionic polarization processes, the force due to external electric field for which movement of internal individual dipoles occurs is balanced by elastic binding forces. The Young's modulus of nickel doped composites being lower than that of the other transition metal ions (Co^{2+} and Cu^{2+}) conjugated mullite composites (Table 2), it can be supposed that elastic binding force which is resistant to polarization processes is lower that leads to higher polarization of the internal dipoles and hence higher dielectric constant in nickel mullite composites.

In dielectrics some interactive forces between adjacent molecules are supposed to exist that try to prevent their orientation according to the external field. This short range interaction force can be suggested to reduce the dielectric constant of the composites. At 1 KHz frequency, in case of cobalt ion doping, the maximum dielectric constant (~98) was obtained for M_{11} and for copper ion, the maximum value of dielectric constant (~34) was achieved for sample M_{33} with a sudden decrease in dielectric constant for 0.03 (M) doping at same frequency. Maxwell-Wagner-Sillars (MWS) interfacial polarization mechanism describes polarizations at the interfaces of alumina, mullite and aluminate phases which may be dominant at lower frequencies like 1 KHz. The dielectric constant of pure mullite (~91) was obtained to be higher than that of other reported ones which may be due to the resulting larger porosity. Formation of elongated grains distributed among equiaxed spherical grains can reduce the interfacial area per unit volume but enhance the resistive interaction force between grains due to larger intersection probability of elongated grains within spherical particles.[45] Since there is no morphological changes occurred for M_{11}, the dielectric constant increased due to larger grains having larger interfacial area per unit volume leading to greater interfacial polarizations. A drop in dielectric constant values was observed for M_{12} since some elongated grains have formed within equiaxed grains resulting in lower interfacial area and larger interaction probabilities that inhibit polarizations. Again an increase in the value of ε occurred for larger interfacial polarization resulting from grain growth followed by final decreased value for agglomeration of grains. The variation of dielectric constant for copper doped mullite composites follow similar pattern to that of cobalt doped samples. The only exception is a drop of ε value for M_{31} which is probably due to formation of interconnected elongated grains. For further doping, dielectric constant increased upto 0.14 (M) doping concentration followed by a decrease for highest doping concentration which can be explained in the same way to that of cobalt doped samples. In case of nickel doped samples, no abrupt

View Article Online
DOI: 10.1039/C5RA21091G

variation of dielectric constant was observed since there is no morphological changes occurred for nickel ion doping. With doping concentration increased upto 0.06 (M), a continuous increase in ε value occurred due to interfacial polarizations at the interfaces of mullite alumina and nickel aluminates. Further doping with nickel ion results in a decrease in ε value and remains almost invariant with higher doping due to exaggerated grain growth.

The tangent loss (tanδ) is indicative of energy dissipation in dielectric system that is proportional to the imaginary part of dielectric constant.[25, 46] Generally loss in the mullite composites happens due to the migration of mobile cations and deformation losses resulting from network constructed by silica.[47] It was reported earlier from Cole-Cole plot of dielectric permittivity that Debye-like relaxation is the most dominating relaxation type which can occur in mullite ceramics.[48] Thus, non-linear increase of tangent losses which was observed for all three transition metal ions doped mullite composite (Figures 9a, 9b and 9c) may be due to different Debye-like relaxations.[49] The increased tangent losses can be caused due to higher ionic conductivity through the oxygen defects formed due to transition metal ion doping whereas lowering of tangent losses occurred for the morphological changes in the composites. [25]
Figure 10 shows the variation of dielectric constant and ac conductivity of mullite with increased doping concentrations of Co^{2+}, Ni^{2+}, Cu^{2+} at 100 Hz, 10 KHz at 1 MHz frequencies.

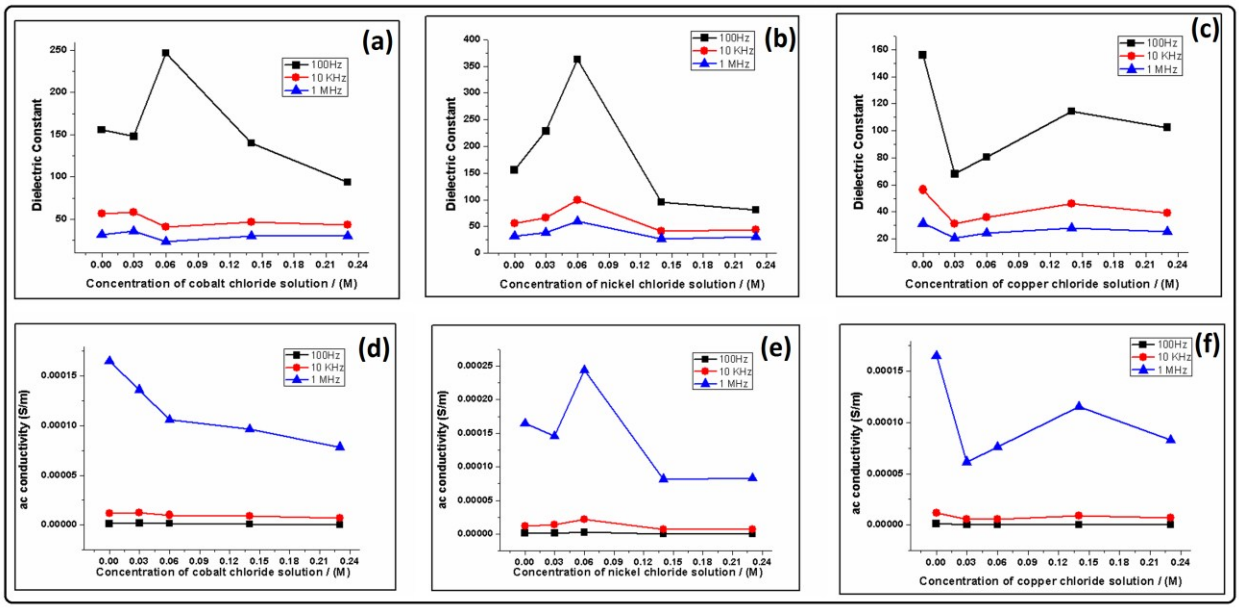

Figure 10: Concentration dependent dielectric constant for (a) Co^{2+}, (b) Ni^{2+} and (c) Cu^{2+} and ac conductivity for (a) Co^{2+}, (b) Ni^{2+} and (c) Cu^{2+} doped mullite composites.

At higher frequencies the variation of dielectric constants are not very prominent due to restricted response of induced dipoles in the composites. Ac conductivities of the composites show the same nature to that of dielectric constant.

3.7.2. : Frequency dependent dielectric properties:

View Article Online
DOI: 10.1039/C5RA21091G

Figures 11a, 11d and 11g show the frequency dependent dielectric constants of Co^{2+}, Ni^{2+}, Cu^{2+} ion doped mullite nanocomposites respectively.

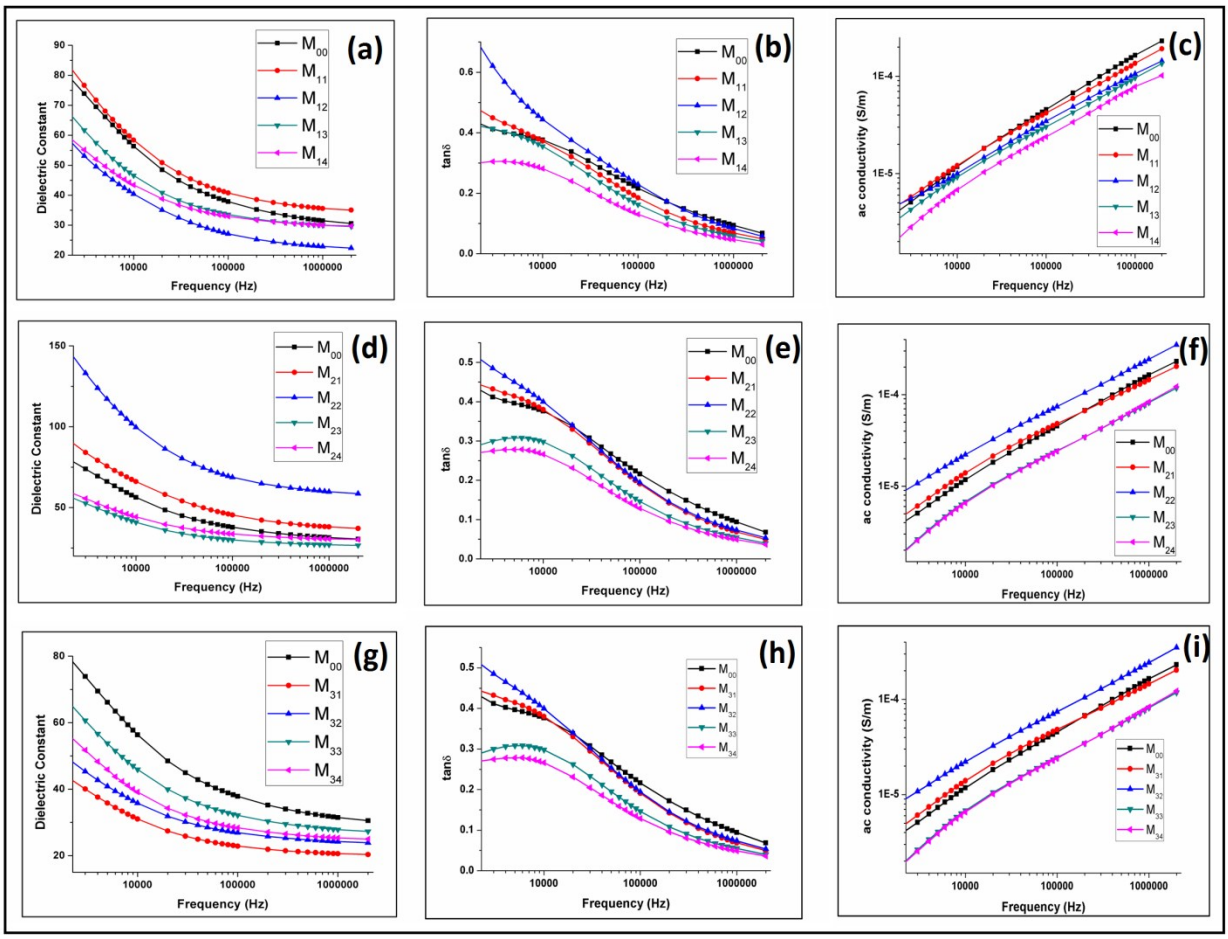

Figure 11: Frequency response of (a) dielectric constant, (b) tangent losses and (c) ac conductivity for pure and Co^{2+} doped mullite composites, (d) dielectric constant, (e) tangent losses and (f) ac conductivity for pure and Ni^{2+} doped mullite composites and (d) dielectric constant, (e) tangent losses and (f) ac conductivity for pure and Cu^{2+} doped mullite composites.

The obvious decrease of dielectric constant with increased frequency is readily attributed to the restricted movement of different polarizations with frequency. The polarization process in transition metal ion doped mullite nanocomposite can be viewed similar to that of conduction processes. Among various conduction mechanisms like Schottky, Poole-Frenkel, Ionic Hopping and Space Charge Limited Current mechanisms, ionic hopping between the oxygen vacancies in mullite structure is responsible for the conduction processes in mullite ceramic composites.[50-52] Doping with transition metals tends to increase this conductivity to several orders of magnitude.[53] The electrical conduction mechanism can be interpreted by electron-hopping model proposed by Heikes and Johnston.[54] The interwell hopping is supposed to contribute for the dielectric relaxation of transition metal-mullite nanocomposite at lower frequencies whereas the dielectric constants of all samples remain almost constant at high frequency range because beyond a

View Article Online
DOI: 10.1039/C5RA21091G

certain frequency of the applied electric field, intrawell hopping becomes predominant and the charge carriers in the composites donot have enough time for long range hopping before the reversal of the external field. As a result, only intrawell hopping exists at high frequency range since the average intrawell hopping distance of the order of one lattice spacing is less than that for interwell hopping which ranges about few nanometres. Therefore, the average polarisation decreases as the frequency is increased resulting in a lowering of dielectric constant at higher signal frequency.

Figures 11b, 11e and 11h show the frequency dependence of tangent losses (tan δ) for Co(II), Ni(II) and Cu(II) doped mullite composites. The loss value was higher at lower frequencies and gradually decreased at higher frequency upto a lower saturated value. The tangent loss being representative of energy dissipation in dielectrics is proportional to the imaginary part of the dielectric constant and depends on the randomness of grain orientation and grain boundaries. The higher value of losses at lower frequencies can be attributed to the favourable movement of dipoles at lower field reversal time and lower value of losses at higher frequency is due to the limited dielectric response. Moreover, at lower frequencies, due to lower conductivity, electrons require more energy for conduction through grains. Therefore, energy dissipation is high at low frequency range resulting in higher tangent losses. At high frequency, higher conductivity leads to exchange of electrons between two conducting grains becomes favourable, resulting a decrease in loss. [47]

The ac conductivities of cobalt nickel and copper ions doped mullite composite have been shown in Figures 11c, 11f and 11i respectively. An increase of conductivity of all samples with increased frequency of the applied field occurred obeying the frequency dependent part of Johnscher's universal power law which is as following:

$$\sigma(\omega) = \sigma_{dc} + \sigma_0 \omega^S$$

where σ_{dc} is the dc conductivity which is frequency independent part and σ_0 is frequency dependent part with S ranging between 0 and 1. The linear increase of conductivities can be correlated directly with Maxwell-Wagner-Sillars (MWS) interfacial space charge polarization effect and dielectric relaxation at higher frequencies. The mobility of transition metal ions and aluminium cations is facilitated in the amorphous phases produced by doping.[25] Due to this higher mobility of charges, cations get an easy path to move resulting in larger conductivity. Moreover, the complex structural rearrangements in mullite composites, ion hopping through oxygen defects and charge conduction via grain boundaries are responsible for higher conductivity of the mullite composites.[47]

3.8. Photoluminescence properties:

The photoluminescence spectra of Co^{2+}, Ni^{2+} and Cu^{2+} doped mullite nanocomposite were obtained with excitation wavelength of 255 nm and shown in Figure 12.

View Article Online
DOI: 10.1039/C5RA21091G

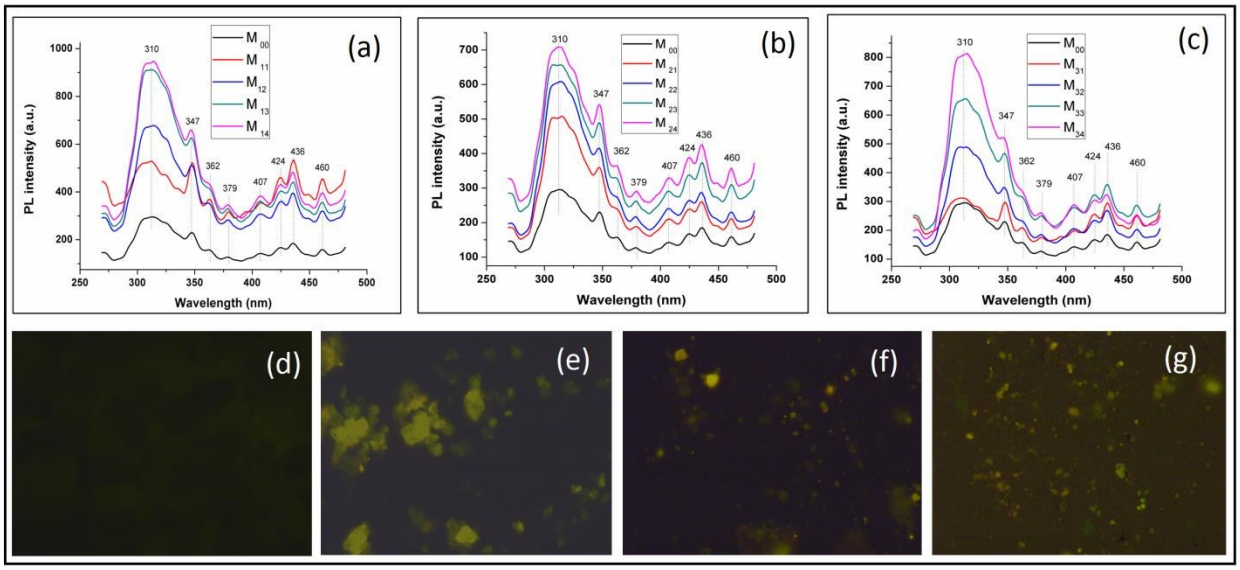

Figure 12: Photoluminescence spectra of pure and (a) Co^{2+}, (b) Ni^{2+} and (c) Cu^{2+} doped mullite nanocomposites with excitation wavelength at 255 nm and fluorescence microscopic images of (d) M_{00}, (e) M_{13}, (f) M_{23} and (g) M_{33} with blue light excitation.

Strong PL bands were observed at 310, 347, 436 and 460 nm with weak bands reflecting at 362, 379, 407 and 424 nm. The radiative centers leading to the PL bands are supposed to be generated from Al-O bonds in mullite bonding structures.[22] The dimensions of the mullite and spinel grains being too higher to show quantum confinement effect,[55] excluding the possibility of PL emission due to a quantum confinement, the observed PL emission bands may be attributed to the oxygen related defects in transition metal-mullite nanocomposites. The PL emissions are expected to result from the radioactive recombination photo-excited holes with electrons occupying the oxygen vacancies. The production of oxygen vacancies in mullite structure is obvious when Si^{4+} lattice sites are replaced by Al^{3+} and the vacancy formation equation is as follows:

$2Si^{4+} + O^{2-} \rightarrow 2Al^{3+} + \otimes$ where $\otimes$ represents oxygen vacancy.[15] Therefore it is obvious that adequate number of oxygen vacancies can be formed in alumina rich mullite structures since large numbers of substitutions occur that result in prominent oxygen defects. The mullite synthesized during our work being silica deficient, it can be ascribed to form definite oxygen vacancies for which even in case pure mullite sample, PL emission bands were visible.

Transition metal ions in their oxide states while react with alumina, can introduce defect structures in mullite which is responsible for PL emissions. The defect reaction can be represented like the following:

$$MO + Al_2O_3 \rightarrow M'_{Al} + Al^{xx}_{Al} + O^{xx}_{O} + \frac{1}{2}V_O^{\cdot\cdot}$$

Where M= Co, Ni or Cu, and V_O designates vacancy.

In solid solution of transition metal oxides and alumina, transition metal oxides dissolve substitutionally and the dopant metal ion will get one negative charge (M'_{Al}) which is

View Article Online
DOI: 10.1039/C5RA21091G

compensated by the formation of positive effective charge or oxygen vacancy. In this defect reactions neutral metal (Al_{Al}^{xx}) and oxygen lattices sites (O_O^{xx}) are also formed in order to maintain charge neutrality.

The higher doping concentration of transition metal ions thus can be attributed to the increase in oxygen vacancy density in the composite structures. This increase in the density of localized defect state in the energy band gap can cause an increase in intensity of PL bands (UV region) and is confirmed by the prominent enhancement of PL intensity around 310 nm at higher doping concentrations.

The fluorescence microscopic images are shown in Figures 12d, 12e, 12f and 12g for M_{00}, M_{13}, M_{23} and M_{33} samples with excitation in blue light. The fluorescence corresponding to pure mullite sample is not very prominent which can be readily predicted from the lower PL intensity. The highest PL intensity of cobalt ion doped mullite composite was reflected from the fluorescence microscopic image of M_{13} possessing highest intensity followed by that of M_{33} and M_{23}.

4. Conclusion:

Multifunctional ceramic composites in terms of transition metal ions conjugated mullite have been developed. The higher densification (~ 99% relative density for nickel ion doping), moderate hardness and Young's modulus due to different ion doping make these composites not only useful in structural application, but also as ceramic pigments in paint systems due to the formation of colored aluminate spinel phases. The highest value of hardness (~8.7 GPa) and Young's modulus (~207 GPa) was found for highest doping concentration of copper and cobalt ions respectively. Higher dielectric constants of pure (~ 91) and metal ions doped mullite composites (~ 175 for 0.06 (M) nickel chloride doping) have revealed a wide scope for these composites in profound electrical applications like ceramic capacitors. Prominent fluorescent properties in both UV and visible region resulting from oxygen defect structures with highest fluorescence intensity obtained for cobalt doped mullite composites make it suitable for optical applications too. Thus, the developed ceramic composites with unique combination of physico chemical, dielectric, mechanical and photoluminescence properties may have promising structural, electrical and optical applications in everyday life.

Acknowledgements

Authors are grateful to DST (INSPIRE PROGRAM (No.: DST/INSPIRE Fellowship/2013/797, Code: IF130870)), Government of India for their financial support.

View Article Online
DOI: 10.1039/C5RA21091G

References

1. D. X. Li and W. J. Thomson, *J. Am. Ceram. Soc.*, 1991, **74**, 2382.
2. A. Kool, P. Thakur, B. Bagchi, N. A. Hoque and S. Das, *Appl. Clay Sci.*, 2015, **114**, 349.
3. I. A. Aksay, D. M. Dabbs and M. Sarikaya, *J. Am. Ceram. Soc.*, 1991, **74**, 2343.
4. M. M. S. Sanad, M. M. Rashad, E. A. Abdel-Aal and M. F. El-Shahat, *Ceram. Int.*, 2013, **39**, 1547.
5. K. Yoshida, H. Hyuga, N. Kondo and H. Kita, *Mater. Sci. Engg. B.*, 2010, **173**, 66.
6. E. Tkalcec, S. Kurajica and H. Ivankovic, *J. Eur. Ceram. Soc.*, 2005, **25**, 613.
7. S. Aryal, P. Rulis and W. Y. Ching, *J. Am. Ceram. Soc.*, 2012, **95**, 2075.
8. C. H. Ruscher, G. Schrader and M. Gotte, *J. Eur. Ceram. Soc.*, 1996, **16**, 169.
9. R. X. Fischer, H. Schneider and D. Voll, *J. Eur. Ceram. Soc.*, 1996, **16**, 109.
10. J. Parmentier and S. Vilminot, *Chem. Mater.*, 1997, **9**, 1134.
11. H. Schneider and S. Komarneni, Mullite. *Wiley-VCH*, Weinheim, 2005.
12. L. S. Cividanes, T. M. B. Campos, L. A. Rodrigues, D. D. Brunelli and G. P. Thim, *J. Sol-Gel. Sci. Technol.*, 2010, **55**, 111.
13. B. Bagchi, S. Das, A. Bhattacharya, R. Basu and P. Nandy, *J. Am. Ceram. Soc.*, 2009, **92**, 748.
14. J. Parmentier and S. Vilminot, *J. Alloys. Compd.*, 1998, **264**, 136.
15. H. Schneider, J. Schreuer and B. Hildmann, *J. Eur. Ceram. Soc.*, 2008, **28**, 329.
16. B. Bagchi, S. Das, A. Bhattacharya, R. Basu and P. Nandy, *J. Sol-Gel. Sci. Technol.*, 2010, **55**, 135.
17. L. B. Kong, H. Huang, T. S. Zhang, Y. B. Gan, J. Ma, F. Boey and R. F. Zhang, *Mater. Sci. Engg. A.*, 2003, **359**, 75.
18. L. B. Kong, T. S. Zhang, J. Ma and F. Boey, *J. Eur. Ceram. Soc.*, 2003, **23**, 2247.
19. E. E. Kiss and P. S. Putanov, *React. Kinet. Catal. Lett.*, 2003, **79**, 325.
20. J. P. Buban, K. Matsunaga, J. Chen, N. Shibata, W. Y. Ching, T. Yamamoto and Y. Ikuhara, *Science*, 2006, **311**, 212.
21. X. S. Peng, L. D. Zhang, G. W. Meng, X. F. Wang, Y. W. Wang, C. Z. Wang and G. S. Wu, *J. Phys. Chem. B.*, 2002, **106**, 11163.
22. H. K. Seong, U. Kim, M. H. Kim and H. J. Choi, *J. Am. Ceram. Soc.*, 2007, **90**, 1937.
23. O. Khatim, T. H. N. Nguyen, M. Amamra, L. Museur, A. Khodan and A. Kanaev, *Acta Mater.*, 2014, **71**, 108.
24. M. A. Camerucci, G. Urretavizcaya, M. S. Castro and A. L. Cavalieri, *J. Eur. Ceram. Soc.*, 2001, **21**, 2917.
25. D. Roy, B. Bagchi, S. Das and P. Nandy, *Mater. Chem. Phys.*, 2013, **138**, 375.
26. S. Roy, S. Kar, B. Bagchi and S. Das, *Appl. Clay Sci.*, 2015, **107**, 205.
27. M. Sales, C. Valentin and J. Alarcon, *J. Eur. Ceram. Soc.*, 1997, **17**, 41.
28. D. Mazza, A. Delmastro and S. Ronchetti, *J. Eur. Ceram. Soc.*, 2000, **20**, 699.
29. S. Kurajica, E. Tkalcec and J. Schmauch, *J. Eur. Ceram. Soc.*, 2007, **27**, 951.
30. P. H. Bolt, F. H. P. M. Habraken and J. W. Geus, *J. Solid. State Chem.*, 1998, **135**, 59.

View Article Online
DOI: 10.1039/C5RA21091G

31. M. Sales, C. Valentin and J. Alarcon, *J. Sol-Gel. Sci. Technol.*, 1997, **8**, 871.
32. M. Sales, J. Vila and J. Alarcon, *J. Mater. Sci.*, 1998, **33**, 4435.
33. D. Chicot, D. Mercier, F. Roudet, K. Silva, M. H. Staia and J. Lesage, *J. Eur. Ceram. Soc.*, 2007, **27**, 1905.
34. T. Martisius and R. Giraitis, *J. Mater. Chem.*, 2003, **13**, 121.
35. A. Kool, P. Thakur, B. Bagchi, U. Rajak, T. Das, S. Kar, G. Chakraborty, T. K. Mukhopadhyay and S. Das, *J. Asian. Ceram. Soc.*, 2014, **2**, 297.
36. P. Padmaja, G. M. Anilkumar, P. Mukundan, G. Aruldhas and K. G. K. Warrier, *Int. J. Inorg. Mater.*, 2001, **3**, 693.
37. M. Zhou, K. Sun and J. Wu, *J. Mater. Sci. Lett.*, 2001, **20**, 2021.
38. J. H. Li, H. W. Ma and W. H. Huang, *J. Hazard. Mater.*, 2009, **166**, 1535.
39. S. M. Naga and A. El-Maghraby, *Mater. Char.*, 2011, **62**, 174.
40. B. R. Lawn and V. R. Howes, *J. Mater. Sci.*, 1981, **16**, 2745.
41. D. B. Marshall, T. Noma and A. G. Evans, *J. Am. Ceram. Soc.*, 1982, **65**, 175.
42. J. Gong, J. Wang and Z. Guan, *Mater. Lett.*, 2002, **56**, 941.
43. M. I. Osendi and C. Baudin, *J. Eur. Ceram. Soc.*, 1996, **16**, 217.
44. D. Ghahremani, T. Ebadzadeh and A. Maghsodipour, *Ceram. Int.*, 2015, **41**, 1957.
45. P. Thakur, A. Kool, B. Bagchi, S. Das and P. Nandy, *Phys. Chem. Chem. Phys.*, 2015, **17**, 1368.
46. M. Jaroszewski, *Eur. Phys. J. B.*, 2015, **88**, 262.
47. K. Halder, D. Roy and S. Das, *J. Mater. Sci. Mater. Electron.*, 2015, **26**, 5803.
48. R. H. M. Van de leur and C. A. P. Zevenhoven, *J. Mater. Sci.*, 1991, **26**, 4086.
49. P. Thakur, A. Kool, B. Bagchi, N. A. Hoque, S. Das and P. Nandy, *Phys. Chem. Chem. Phys.*, 2015, **17**, 13082.
50. R. Kaur, C. Singh, V Bhikhan, M. Jaroszewski and S. Bindra Narang, *Eur. Phys. J. B.*, 2015, **88**, 245.
51. G. Mata-Osoro, J. S. Moya, M. Morales, L. A. Diaz, H. Schneider and C. Pecharromán, *Int. J. Mater. Res.* 2012, **103**, 408.
52. S. P. Chaudhuri, S. K. Patra and A. K. Chakraborty, *J. Eur. Ceram. Soc.*, 1999, **19**, 2941.
53. C. Neusel, H. Jelitto and G. A. Schneider, *J. Appl. Phys.*, 2015, **117**, 154902.
54. R. Heikes and D. R. Johnston, *J. Chem. Phys.*, 1957, **26**, 582.
55. C. Liang, G. Meng, Y. Lei, F. Phillipp and L. Zhang, *Adv. Mater.*, 2001, **13**, 1330.

View Article Online
DOI: 10.1039/C5RA21091G

Figure Captions:

Figure 1: A schematic diagram for the preparation of transition metal ions conjugated mullite nanocomposites.

Figure 2: A comparative powder X-ray diffraction pattern of pure and (a) Co^{2+}, (b) Ni^{2+} and (c) Cu^{2+} doped mullite nanocomposite sintered at 1300^{o}C.

Figure 3: Fourier transform infrared spectra of pure and (a) Co^{2+}, (b) Ni^{2+} and (c) Cu^{2+} doped mullite nanocomposites sintered at 1300^{o}C.

Figure 4: Field emission scanning electron micrographs of (a) pure mullite (M_{00}), cobalt doped mullite (b) M_{11}, (c) M_{12}, (d) M_{13} and (e) M_{14}, nickel doped mullite (f) M_{21}, (g) M_{22}, (h) M_{23} and (i) M_{24} and copper doped mullite (j) M_{31}, (k) M_{32}, (l) M_{33} and (m) M_{34}.

Figure 5: Densification behavior and variation of apparent porosity of mullite doped with (a) Co^{2+}, (b) Ni^{2+} and (c) Cu^{2+}.

Figure 6: Digital images for the pellets of pure and transition metal ions conjugated mullite composites after sintering at 1300^{o}C.

Figure 7: Plots of (a) $(H_K)_{TAC}$ v/s H_V and (b) s/L v/s $H_V/(H_K)_{TAC}$

Figure 8: Variation of (a) hardness and (b) Young's modulus with doping concentration of transition metal ions

Figure 9: Doping concentration dependent dielectric constant and tangent losses of mullite composite doped with (a) Co^{2+}, (b) Ni^{2+} and (c) Cu^{2+} at 1 KHz frequency.

Figure 10: Concentration dependent dielectric constant for (a) Co^{2+}, (b) Ni^{2+} and (c) Cu^{2+} and ac conductivity for (a) Co^{2+}, (b) Ni^{2+} and (c) Cu^{2+} doped mullite composites.

Figure 11: Frequency response of (a) dielectric constant, (b) tangent losses and (c) ac conductivity for pure and Co^{2+} doped mullite composites, (d) dielectric constant, (e) tangent losses and (f) ac conductivity for pure and Ni^{2+} doped mullite composites and (d) dielectric constant, (e) tangent losses and (f) ac conductivity for pure and Cu^{2+} doped mullite composites.

Figure 12: Photoluminescence spectra of pure and (a) Co^{2+}, (b) Ni^{2+} and (c) Cu^{2+} doped mullite nanocomposites with excitation wavelength at 255 nm and fluorescence microscopic images of (d) M_{00}, (e) M_{13}, (f) M_{23} and (g) M_{33} with blue light excitation.

Table Captions:

Table 1: Description of prepared samples along with their designations

Table 2: Particle size from Debye-Scherrer's equation, relative density, apparent porosity, dielectric constant, hardness and Young's modulus for pure and transition metal ions doped mullite composites.

View Article Online
DOI: 10.1039/C5RA21091G

Mechanical, dielectric and photoluminescence properties of transition metal ions doped mullite nanocomposite synthesized via alkoxide hydrolysis.